PAPER

Check for updates

Ultrasonic decoating as a new recycling path to separate oxygen side layers of solid oxide cells†

Carlo Kaiser, (ID) * Thomas Buchwald and Urs A. Peuker

Hydrogen is considered the most promising solution for the energy transition. To meet the future demand for green hydrogen, electrolyzers are a key technology. Among the established electrolyzers, solid oxide electrolyzers have the highest electrical efficiency and are the subject of intensive research. However, the core of solid oxide electrolyzers, the solid oxide cells (SOC), require a significant amount of critical raw materials, making recycling of these materials crucial. Initial recycling approaches rely on expensive manual labor or hydrometallurgical approaches that generate environmentally hazardous residues. This study investigates ultrasonic decoating as an alternative recycling approach. Ultrasonic decoating is simple, can be automated, and does not require additional hazardous materials. For the study, decoating experiments were performed on different SOC with varying sonication times. The quality of SOC decoating was evaluated by optical image analysis using a decoating efficiency. The chemical composition of the removed particles was investigated to draw conclusions about the selectivity. Overall, it was shown that ultrasonic decoating is a suitable recycling approach to separate the oxygen side layers, the perovskites, of SOC. Complete and selective liberation and separation of the oxygen side layers can be achieved by ultrasonic decoating.

Introduction

The European Union (EU) has committed itself to achieving climate neutrality by 2050.[1] In this context, a transition from fossil fuels to renewable energy sources is essential. The most promising approach to contribute to the energy transition is green hydrogen, as it can be stored, easily transported and be produced from green electricity and water.[2,3] In order to meet the future demand for hydrogen required for the energy transition, it will be necessary to produce hydrogen on a large scale using electrolyzers.[4,5] In this context, global electrolyzer capacity is expected to increase from 700 MW at the end of 2022 to 175–420 GW by 2030, based on announced projects.[6] The three types of water electrolyzers that are currently the most technologically advanced are: alkaline electrolyzers, polymer exchange membrane electrolyzers, and solid oxide electrolyzers (SOEL).[6] With conversion efficiencies of up to 90% and more – without the presence of precious metals – SOEL has become of interest to many researchers.[7–9] However, its high operating temperatures of 600–850 °C cause high material stress and eventually a short lifetime of about 2–3

years.[10–12] Therefore, it is essential to have an appropriate recycling strategy as the demand for SOEL increases in terms of quantity.[13–16]

There is currently a lack of established technologies for recycling SOEL and the corresponding fuel cells.[13,14] SOEL contain several materials that are on the EU's list of critical materials,[17] such as rare earth elements and nickel.[12,18] Especially in the core element, the solid oxide cells (SOC), where the reaction of water to hydrogen and oxygen takes place, several critical materials are used. These materials are distributed throughout the three layered parts of the cell: hydrogen side, oxygen side, and intermediate electrolyte. Various SOC cell designs exist, but electrolyte-supported and hydrogen-electrode-supported cells are the most commonly used as noted in studies.[12,18–20] Based on the different cell designs, oxide materials with a fluorite structure such as cubically stabilized zirconia and doped ceria are considered state-of-the-art (SoA) for the electrolyte.[21] Yttrium-stabilized zirconia (YSZ) is commonly used for hydrogen-electrode-supported cells due to its affordability, while scandium-stabilized zirconia (ScSZ) has a higher ionic conductivity and is more suitable for electrolyte-supported cells.[18,21] On the hydrogen side, a cermet of Ni and electrolyte material is generally used.[12] For the oxygen side, perovskite-type materials of the formula ABO_3 are used.[12] The most commonly used perovskite materials are lanthanum-containing, *i.e.*, $La_{1-x}Sr_xCo_{1-y}Fe_yO_{3-\delta}$ (LSCF), $La_{1-x}Sr_xCoO_{3-\delta}$ (LSC) and $La_{1-x}Sr_xMnO_{3-\delta}$ (LSM).[12,18,21] The

Institute of Mechanical Process Engineering and Mineral Processing, TU Bergakademie Freiberg, 09599 Freiberg, Germany.
E-mail: Carlo.Kaiser@mvtat.tu-freiberg.de
†Electronic supplementary information (ESI) available. See DOI: https://doi.org/10.1039/d3gc03189f

reaction at the electrodes requires a combination of ionic conductivity and electrical conductivity,[10] and LSCF and LSC meet these requirements.[22] However, LSCF and LSC tend to react with the zirconia in the electrolyte during sintering, for which a gadolinium-doped ceria (GDC) reaction barrier is used to separate these layers.[12,23] LSM, on the other hand, is chemical stable but has negligible ionic conductivity.[12,24,25] Therefore, its composite with stabilized zirconia is used in oxygen electrodes.[18]

Based on the materials used and the structure of the cells, there are first approaches for recycling. A first recycling strategy has been published by Sarner et al.[21] According to Sarner et al., different cell designs require different recycling steps, but regardless of the cell design, the first step is to separate the oxygen side. As a possible option, they emphasize hydrometallurgical methods, since high purities of the separated fraction are required for successful reuse. On the other hand, hydrometallurgy requires large amounts of acids or organic solvents, which generate environmentally hazardous residues. A starting point for a hydrometallurgical process for oxygen side recycling was provided by Benedetto Mas et al.[26] They reviewed the literature for methods to leach lanthanum and cobalt from waste materials. The aim was to provide guidance in defining experimental conditions for an efficient and green process to recycle lanthanum and cobalt from perovskite materials from SOC. The first recycling process for SOC with a focus on YSZ recovery was carried out by Saffirio et al.[27] First, layers containing YSZ were isolated. This involved removal of the oxygen side by hand scratching with a spatula and polishing away the GDC reaction barrier. The remaining Ni-YSZ material was then mechanically crushed, sieved and further disaggregated by hydrothermal treatment. Finally, Ni was removed by leaching with HNO_3, leaving YSZ. Although the YSZ material obtained at the end of the process meets the requirements for re-use in cells, there is still room for a significant increase of the technical readiness level especially in the mechanical processes due to the long grinding times and the manual work involved. An alternative SOC recycling process was developed by Sarner et al.[28] Their concept was a semi-closed recycling loop for hydrogen electrode supported cells. In the first step, nickel was oxidized to nickel oxide to provide greater resistance to inorganic acid leaching. The oxidized cells were then leached in 20% dilute HCl to separate the perovskites. The cells without the oxygen side were milled, mixed with new material, and then processed into new hydrogen-supported substrates. Even though separating the perovskites stated in this process with leaching is easy to scale up in comparison to manual scraping and polishing, it still relies on acids, which generate environmentally hazardous residues.

To reduce the manual effort and avoid additional hazardous materials, an automated mechanical process for selective separation of the oxygen side is necessary. Due to the layered structure of SOC, decoating approaches are advantageous for recovering highly concentrated material streams. A decoating method that has already successfully been tested by Lei et al. for the recycling of lithium-ion batteries is ultrasonic decoating.[29] They showed that cavitation caused by high-intensity ultrasonication breaks the adhesive bonds between the metal foil and the coating of lithium-ion batteries. According to Lei et al., high material recovery and throughput rates, along with ease of process scale-up, are possible through the use of ultrasonic decoating.

Based on these results, the current study has tested ultrasonic decoating for the first step of SOC recycling. The goal was to completely and selectively separate the oxygen side layers of the cell. In a preliminary study, the influence of the spacing between the sonotrode and the cell on the decoating behavior was investigated. This was followed by tests with different exposure times to determine the decoating efficiency and selectivity of the ultrasonic decoating process.

Experimental and methods

Materials

Three cell types, consisting of the considered SoA materials with different oxygen side designs, were investigated, as shown in Fig. 1. The two cell types on the left are hydrogen-electrode-
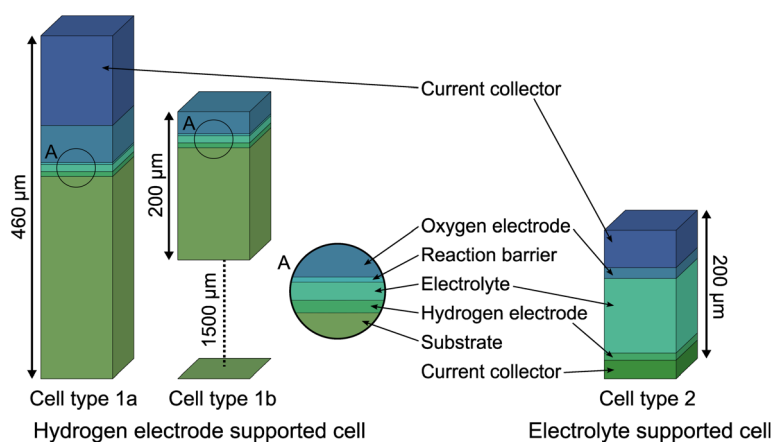

Fig. 1 Schematic structure of the three used SOC cell types and corresponding cell designs.

supported types from different manufacturers. They consist of $La_{0.58}Sr_{0.4}Co_{0.2}Fe_{0.8}O_{3-\delta}$ as oxygen electrode, GDC as reaction barrier, YSZ as electrolyte and a Ni/YSZ cermet as hydrogen electrode and substrate. The current collector layer of cell type 1a is LCC10 ($LaMn_{0.45}Co_{0.35}Cu_{0.2}O_{3-\delta}$).

Cell type 2 is an electrolyte-supported cell. The current collector layer on the oxygen electrode is made of $La_{0.78}Sr_{0.2}MnO_{3-\delta}$. A composite of $La_{0.78}Sr_{0.2}MnO_{3-\delta}$ and YSZ, ScSZ, a composite of GDC and Ni, and Ni are used for the oxygen electrode, electrolyte, hydrogen electrode, and current collector of the hydrogen electrode, respectively.

Ultrasonic setup

Fig. 2 shows the schematic setup for ultrasonic decoating. A cell piece with the perovskite layer facing upwards is fixed underneath the sonotrode. The area of the cell piece is chosen to be larger than twice the sonotrode area. The sonotrode is a Bandelin electronic UW 2200 with a maximum power of 200 W and a diameter of 12 mm. Since the cell is very brittle, it was fixed in a beaker with an N52 neodymium magnet of 10 mm diameter to simplify the preparation and to avoid inducing possible fractures due to mechanical prestress potentially generated by any mechanical fixings. Although the magnetic fixation allows a slight movement of the sample, in case of a breakage of the cell piece, a continuous stress of the fragments under the sonotrode is ensured. Due to the low Curie temperature of LSM[30] the outer beaker, which provides stabilization during ultrasonic stress, is filled with water to cool the inner process water. The amount of water in the inner beaker was 25 ml. The power was set to 160 W. In initial tests, this performance showed high decoating success without introducing too much stress on the cell and causing fractures.

As a preliminary series of tests, the spacing between the sonotrode and the sample was investigated. The goal was to find an optimal distance to achieve the desired decoating and to avoid breaking the cell. The distance was varied between 2, 3 and 4 mm. At a smaller distance of 1 mm, cell fragmentation occurred. Due to small sample quantities, the sonotrode-

sample spacing was not investigated for cell type 1b. Since cell type 1b has a thicker substrate and therefore greater stability, no cell breakage is expected. To ensure consistency for future experiments, the same optimized spacing was used as for cell type 1a. For cell type 1a, the time was set to 30 s, while for cell type 2, which has a higher resistance to ultrasound exposure on the oxygen side, the time was set to 120 s.

Furthermore, the sonication time t was investigated. For the experiments with cell types 1a and 1b, 5 s, 10 s and 30 s were used. Due to the effective decoating behavior of cell type 1a, a further test at 15 s was added. Since cell type 1b did not show a desired decoating even after 30 s, another experiment was conducted at 60 s. Cell type 2 was not investigated further due to the results from the sonotrode-sample spacing investigation.

Characterization of decoating

The decoating efficiency is used for the quantitative evaluation of the decoating success. Since the samples are cell pieces with varying areas, the total area of the sample cannot be used as a reference value. Instead, the sonotrode cross-sectional area A_S is used as the reference. Thus, the sonotrode area-related decoating efficiency E_D is determined as follows:

$$E_D = \frac{A_D}{A_S} \quad (1)$$

A_D refers to the decoated area that has been completely cleaned of its coating. As the reference area is the sonotrode cross section, a decoating efficiency of more than 100% is possible. By the way of comparison, the stressed area $A_{Stressed}$, *i.e.* the area where part of the coating has already come off, is described by the stressed area fraction $E_{Stressed}$ as follows:

$$E_{Stressed} = \frac{A_{Stressed}}{A_S} \quad (2)$$

The decoated area is determined by image analysis illustrated in Fig. 3. Images were captured with a Bresser DST-1028 5.1 MP USB digital microscope and analyzed using Fiji (ImageJ 2.3.0).[31] For cell type 1a, the thresholding method was used for segmentation (Fig. 3a). Due to the contrast between the completely decoated and coated regions, these regions can be distinguished by their color values. Pixels that have a high green value or are dark are considered to be background and coated cell area respectively, while non-green and light pixels are considered to be decoated cell area.

Cell type 1b, on the other hand, showed little contrast between individual areas after stressing. However, a sharp edge between the coated and stressed area was observed in SEM images. For a more detailed investigation of this edge, the surface topography was examined using a laser scanning microscope. It was found that the difference between the outer and inner surfaces through an edge is equal to the nominal thickness of the coating. Therefore, this inner area is considered to be decoated. The edge, *i.e.*, the contour of the decoated area, was determined by contour extraction (Fig. 3b). The manual post-processing of the images, such as the
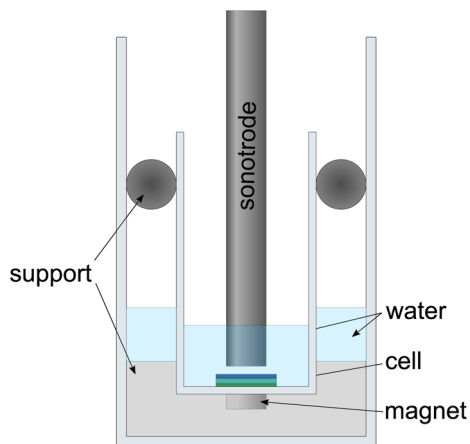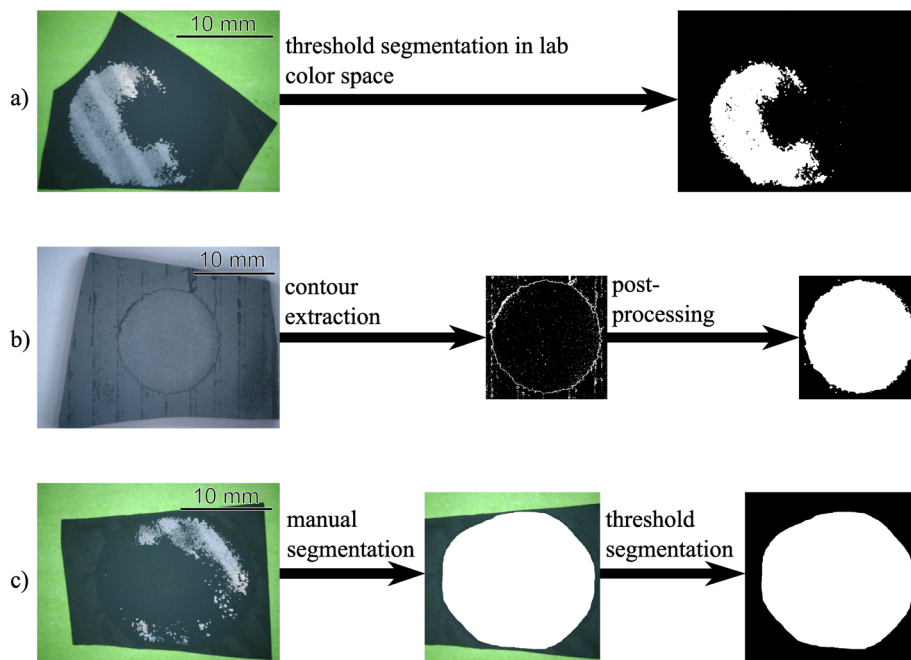

Fig. 2 Schematicsetup for ultrasonic decoating.

Fig. 3 Workflow to segment (a) the decoated area from the coated area for SOC with good contrast between both areas (b) the decoated area from the coated area for SOC with poor contrast between both areas but sharp contour line (c) areas with poor contrast and no sharp contour line.

removal of false contours, completion of the individual contour lines, and filling of the decoated areas, was necessary to determine the decoated area.

The segmentation algorithms were unable to determine the stressed area of cell type 1a and cell type 2, as well as the decoated area of cell type 2, by automated image processing. These areas were therefore manually annotated on the images and evaluated (Fig. 3c). The values obtained in this way are only considered as estimates in further discussion due to the possibility for large errors.

In some experiments, fracturing of the cell piece occurred during ultrasound exposure. Due to the magnet, these fragments are held under the sonotrode and stressed further. For this reason, all fragments were considered for the decoating efficiency in the subsequent evaluation.

During sample preparation, initial surface damage occurred at some cell pieces. As a result, edge areas had already been decoated before stressing. In order to include this in the evaluation, an image was taken of each specimen before ultrasonic exposure, which was evaluated using the same methodology as after exposure. The areas affected by stress were corrected using the values obtained before the stress was applied.

Another evaluation criterion for decoating was the decoated particle mass m_P. The samples were weighed before and after stressing and the mass of particle removed was calculated as the difference between the two weights. The composition of the detached particles was then determined using inductively coupled plasma optical emission spectroscopy (ICP-OES). A mixture of hydrochloric and hydrofluoric acid was used to dissolve the particle product.

The mass-specific decoating energy e_m is used for the energetic evaluation of the process. This is determined at a constant sonotrode power P_S as follows:

$$e_m = \frac{P_S \times t}{m_P} \qquad (3)$$

Results and discussion

Sonotrode-sample spacing

As a preliminary test, the influence of the spacing between the sonotrode and the surface of the cell piece was investigated. The results for 2, 3 and 4 mm spacing for cell type 1a and 2 are depicted in Fig. 4 and 5, respectively. The decoating efficiency for cell type 1a decreases significantly with the increasing distance to the sonotrode. At a distance of 2 mm, the decoating efficiency reaches about 160%, while it drastically decreases to below 10% when the distance is increased to 4 mm. Although decreasing the spacing reduces the stress intensity, which can be inferred from the decoating efficiency, the cell piece breaks at all spacings. For the reason of better decoating performance, a distance of 2 mm between sonotrode and sample was chosen for further investigations of cell type 1a.

The decoating efficiency and the stressed area fraction for cell type 2 could only be estimated roughly as there was almost no contrast between coated and decoated areas, and no clear edge between them. Moreover, the small thickness of the cell resulted in increased cell breakage. The curve shows that the
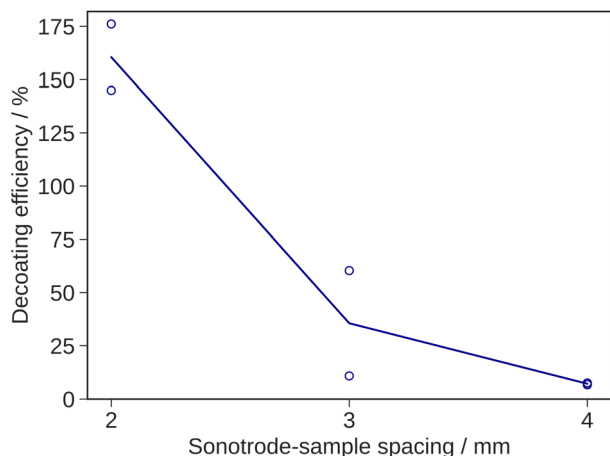
Fig. 4 Decoating efficiency for cell type 1a after stressing for 30 s with 160 W using varying spacing between sonotrode and sample.
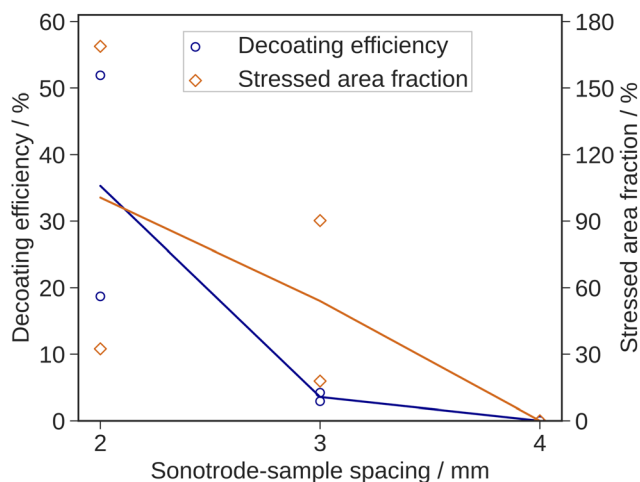

Fig. 5 Estimated decoating efficiency and stressed area fraction for cell type 2 after stressing for 60 s with 160 W using varying spacing between sonotrode and sample.

decoating works much better at a distance of 2 mm than at larger distances. At a distance of 4 mm, no surface damage was detected. It is also noticeable that the decoating efficiency of cell type 2 is lower than that of cell type 1a. This could be due to differences in materials, operating conditions and manufacturing conditions. In addition, cell type 2 uses a composite structure of LSM and YSZ as the oxygen electrode. As the YSZ and the electrolyte of the ScSZ are very similar, a stronger bond can be expected here.

The stressed area fraction shows the same trend as the decoating efficiency, *i.e.* the decoating is more effective at smaller distances. It is noticeable that the values of the points at 2 mm and 3 mm are both far apart. The measuring points with a higher stressed area fraction belong to cell pieces that are broken down into more and smaller fragments compared to those with a lower fraction. The additional fragments create an additional frictional stress between the fragments during ultrasonic exposure. This could be beneficial for the decoating behavior. However, further research would be required to confirm this. In this study, the multiple fractures of the cell pieces lead to a high evaluation effort. In addition, the decoating efficiencies are in the low range, so that ultrasonic decoating in the form investigated here is not effective for cell type 2. For these two reasons, cell type 2 was not investigated further in this study.

Sonication time

Fig. 6 shows the results of ultrasonic decoating for varying sonication times for cell type 1a. Fig. 6a shows the time variation of the decoating efficiency and the corresponding stressed area fraction. The decoating efficiency increases almost linearly until it reaches about 160% at 30 s. Assuming that the sonotrode covers the entire cell surface either sequentially or all at once during the decoating process, a decoating efficiency of approximately 100% would be sufficient. This is achieved after an average of 20 s for cell type 1a. The stressed
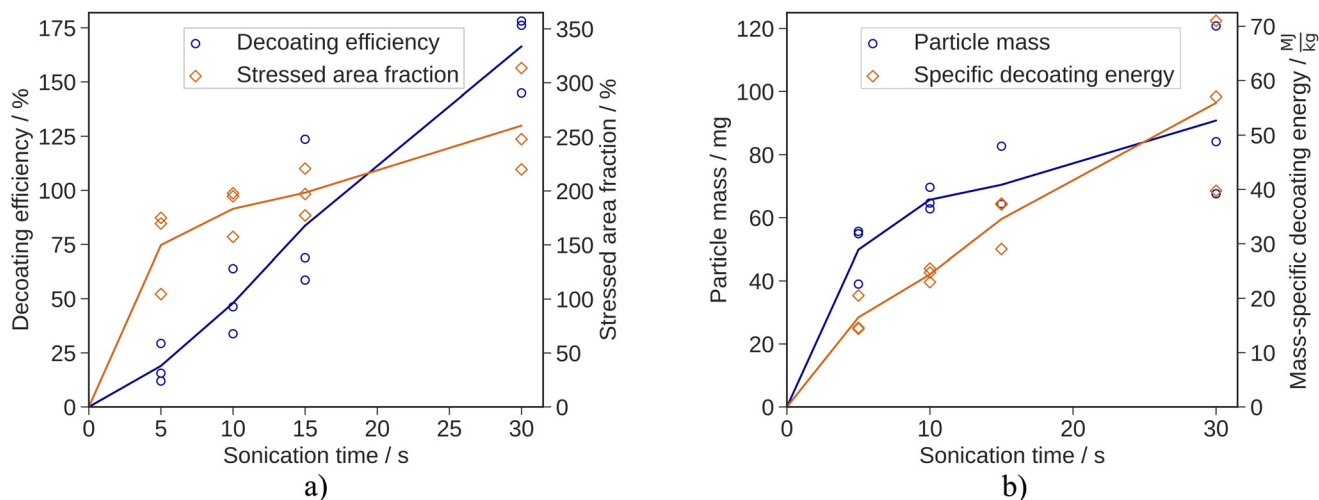

Fig. 6 Ultrasonic decoating results for cell type 1a at varying sonication times: (a) decoating efficiency and estimated stressed area fraction (b) detached particle mass and corresponding energy.

area fraction increases rapidly in the first 5 s followed by a linear trend with a smaller slope. A similar trend can be seen for the removed particle mass in Fig. 6b.

Since the decoating efficiency increases continuously with increasing sonication time, while the stressed area fraction and the decoated particle mass almost stagnate, it can be concluded that the decoating of the oxygen electrode near the interface to the reaction barrier requires particularly high energy. This is complemented by the mass-specific energy input in Fig. 6b, where the mass-specific energy input increases continuously, so that the lowest energy per removed particle mass has to be applied at 5 s, while the decoating efficiency is still low at 20%.

The composition, the purity respectively, of the particle product was investigated by ICP-OES; the elements from the cell except those from the oxygen side are listed in Table 1. The reaction barrier accounts for the largest proportion of contamination, but also material from the opposite hydrogen side was detected. Even with highest level of contamination from all measurements, the value of impurities of the particle product is about 0.4 wt%. Taking the oxygen in YSZ and GDC stoichiometrically into account, the value is corrected to

approximately 0.49 wt%. Ultrasonic decoating is thus very selective for the separation of the oxygen side for cell type 1a.

The results of ultrasonic decoating for cell type 1b with varying sonication times are shown in Fig. 7. As the detachment of the oxygen side particles leads directly to complete decoating, Fig. 7a only displays the decoating efficiency. In the first 10 s, the decoating efficiency hardly increases, then there is a very steep increase up to 30 s until it ends at 60 s at about 100%. The decoating efficiency seems to stagnate at about 100%. This differs from cell type 1a, where the decoating efficiency is well above 100% (*cf.* Fig. 6a). Cell type 1b has a much thicker substrate than cell type 1a and therefore a larger volume of ferromagnetic nickel. This leads to a stronger attraction between the magnet and the cell. The result is a more stable fixation of the cell during ultrasound and thus a more precise stressing. The same trend as the decoating efficiency for cell type 1b can also be seen for the removed particle mass in Fig. 7b. The particle mass hardly increases in the first 10 s, followed by a sharp increase up to 30 s until the curve levels off at approx. 13 mg at 60 s.

This is probably because the surface of the SOC is damaged first, resulting in a larger, more vulnerable and predamaged surface. Consequently, the surface detaches more easily. A look at the curve for the mass-specific energy input in Fig. 7b shows that there is a minimum from an energy point of view. This minimum is about 30 s for the time points considered. Thus, at this time, the lowest energy per particle mass removed has been expended. However, the decoating efficiency is only about 80% on average (see Fig. 7a). A sonication time of 60 s, at which an average decoating efficiency of 100% is achieved, is only slightly higher in terms of energy per particle mass removed than the 30 s time point and even lower than the 5 s and 10 s time points. This point is therefore favorable from the point of view of the specific energy used, but also results in a complete detachment of the layer. Whether an
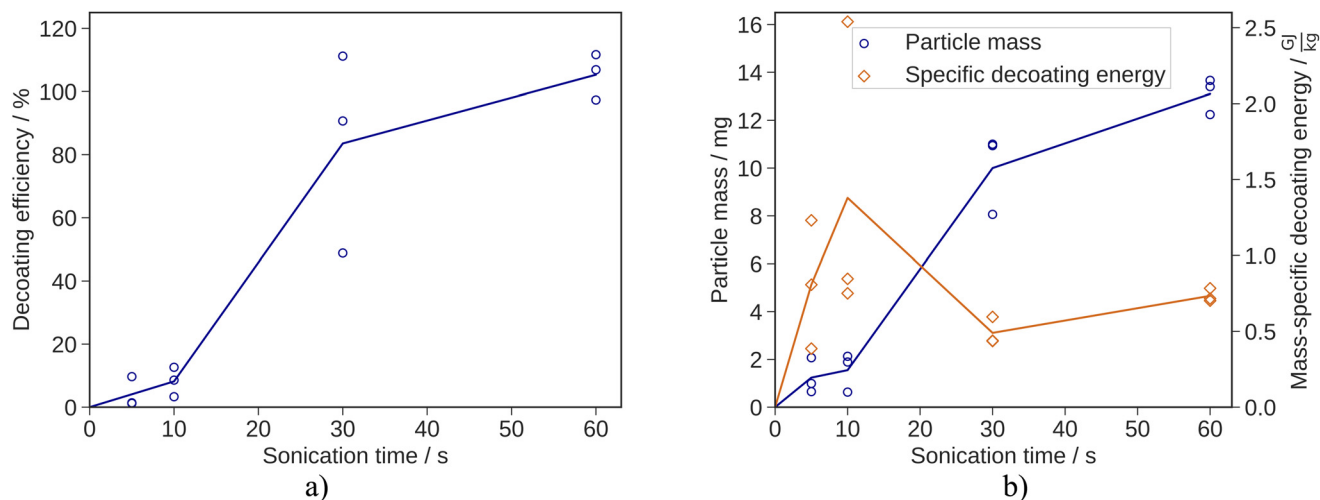
Table 1 Elements other than oxygen side elements detected by ICP-OES from detached particles *via* ultrasonication from cell type 1a and corresponding layer

Element	Wt%	Layer
Ni	0.014–0.060	Hydrogen side
Y	0.001–0.006	Hydrogen side, electrolyte
Zr	0.003–0.057	Hydrogen side, electrolyte
Ce	0.027–0.253	Reaction barrier
Gd	0.004–0.031	Reaction barrier
Σ	0.048–0.407	

Fig. 7 Ultrasonic decoating results for cell type 1b at varying sonication times: (a) decoating efficiency (b) detached particle mass and corresponding energy.

Table 2 Elements other than oxygen side elements detected by ICP-OES from detached particles *via* ultrasonication from cell type 1b and corresponding layer

Element	Wt%	Layer
Ni	0.185–0.238	Hydrogen side
Y	0.030–0.040	Hydrogen side, electrolyte
Zr	0.180–0.240	Hydrogen side, electrolyte
Ce	0.388–0.516	Reaction barrier
Gd	0.274–0.303	Reaction barrier
Σ	1.057–1.337	

even more energetically favorable point with complete separation lies in the range between 30 s and 60 s cannot be said from the data. This would have to be specifically investigated.

The chemical analysis of the removed particles in Table 2 shows that the impurities from the remaining layers are in the range of 1 wt%. The maximum contamination from the measurements is about 1.35 wt%. With stoichiometric consideration of the oxygen in YSZ and GDC, the value is below 1.6 wt%. The reaction barrier accounts for the largest proportion of contamination. Thus, ultrasonic decoating is selective for the oxygen side for cell type 1b as well.

Overall, it can be said that cell type 1a can be decoated more efficiently than cell type 1b. Although the oxygen electrode and the underlying layer are made of the same materials in both cases, there are differences in the decoating behavior, in the material bonding respectively. This is probably due to the manufacturing and operating conditions. However, as these are not known for both cell types, no statement can be made in this study. Therefore, further research is needed to determine how to speed up the decoating and whether manufacturing and operating conditions can be influenced for better recyclability without compromising the functionality of the cells in operation. Both decoated SOC investigated (cell types 1a and 1b) could be of interest as a substrate for new hydrogen electrode supported SOC, comparable to the process described by Sarner *et al.*[28] Further studies are needed to determine if and to what extend additional process steps are required before reuse. For material reuse independent of the cell design, the process of Saffirio *et al.*[27] could be considered. In their process, ultrasonic decoating would replace manual scraping of the oxygen side layers. The reuse of the ablated perovskite powders after ultrasonic decoating requires further investigation. Potentially, a single perovskite material could be reused in the oxygen side layers of new SOC. Perovskite mixtures could be reused as oxygen side current collector layers or would need to be separated in a further step prior to reuse.

Conclusions

This study has shown that as the first step of SOC recycling, decoating the oxygen side by ultrasonic decoating is effective. As an alternative to the manual mechanical and hydrometallurgical processes already investigated, ultrasonic decoating provides a technical approach for selective liberation and separation of the oxygen side that could be automated without the use of environmentally hazardous substances. Complete separation of the oxygen side of the area below the sonotrode can be achieved. The required stress duration depends on the cell type. This needs to be investigated in further studies. The ablated layer had high purities in the range of 98.4 wt% and higher, with the largest contamination caused by the adjacent layer. Due to the thin thickness of the cells, fracture of the cells can occur under stress. Magnetic fixation has been shown to be beneficial, as it allows the cell fragments to be further stressed. Cell pieces that had been broken several times even showed particularly good decoating in some cases. The stress caused by friction between the fine cell particles could improve the decoating.

Conflicts of interest

There are no conflicts to declare.

Acknowledgements

References

1 G. Kakoulaki, I. Kougias, N. Taylor, F. Dolci, J. Moya and A. Jäger-Waldau, *Energy Convers. Manage.*, 2021, **228**, 113649.

2 A. Kovač, M. Paranos and D. Marciuš, *Int. J. Hydrogen Energy*, 2021, **46**, 10016–10035.

3 C. Quarton, *Doctor of Philosophy*, University of Barth, 2021.

4 R. S. El-Emam and H. Özcan, *J. Cleaner Prod.*, 2019, **220**, 593–609.

5 T. Capurso, M. Stefanizzi, M. Torresi and S. M. Camporeale, *Energy Convers. Manage.*, 2022, **251**, 114898.

6 International Energy Agency, *Global Hydrogen Review 2023*, 2023.

7 Y. Zheng, Z. Chen and J. Zhang, *Electrochem. Energy Rev.*, 2021, **4**, 508–517.

8 M. Shen, F. Ai, H. Ma, H. Xu and Y. Zhang, *iScience*, 2021, **24**, 103464.

9 J. Zamudio-García, L. Caizán-Juanarena, J. M. Porras-Vázquez, E. R. Losilla and D. Marrero-López, *J. Power Sources*, 2022, **520**, 230852.

10 A. Hauch, R. Kungas, P. Blennow, A. B. Hansen, J. B. Hansen, B. V. Mathiesen and M. B. Mogensen, *Science*, 2020, **370**, 6513.

11 X. Sun, M. Chen, Y.-L. Liu and P. V. Hendriksen, *ECS Trans.*, 2015, **68**, 3359–3368.

12 A. Nechache and S. Hody, *Renewable Sustainable Energy Rev.*, 2021, **149**, 111322.

13 A. M. Férriz, A. Bernad, M. Mori and S. Fiorot, *Int. J. Hydrogen Energy*, 2019, **44**, 12872–12879.

14 A. Valente, D. Iribarren and J. Dufour, *Int. J. Hydrogen Energy*, 2019, **44**, 20965–20977.

15 E4tech (UK) Ltd for FCH 2 JU in partnership with Ecorys and Strategic Analysis Inc., *Study on Value Chain and Manufacturing Competitiveness Analysis for Hydrogen and Fuel Cells Technologies*, FCH contract 192, September 2019.

16 U. S. Department of Energy, *Water Electrolyzers and Fuel Cells Supply Chain*, 2022.

17 European Commission, *Study on the Critical Raw Materials for the* EU 2023 - Final Report.

18 D. Udomsilp, C. Lenser, O. Guillon and N. H. Menzler, *Energy Technol.*, 2021, **9**, 2001062.

19 S. Harboe, A. Schreiber, N. Margaritis, L. Blum, O. Guillon and N. H. Menzler, *Int. J. Hydrogen Energy*, 2020, **45**, 8015–8030.

20 K. A. Kuterbekov, A. V. Nikonov, K. Z. Bekmyrza, N. B. Pavzderin, A. M. Kabyshev, M. M. Kubenova, G. D. Kabdrakhimova and N. Aidarbekov, *Nanomaterials*, 2022, **12**, 1059.

21 S. Sarner, A. Schreiber, N. H. Menzler and O. Guillon, *Adv. Energy Mater.*, 2022, **12**, 2201805.

22 L. Blum, L. G. J. de Haart, J. Malzbender, N. H. Menzler, J. Remmel and R. Steinberger-Wilckens, *J. Power Sources*, 2013, **241**, 477–485.

23 O. Guillon, *Int. J. Ceram. Eng. Sci.*, 2021, **3**, 100–104.

24 S. P. Jiang, *Int. J. Hydrogen Energy*, 2019, **44**, 7448–7493.

25 Y. Wang, W. Li, L. Ma, W. Li and X. Liu, *J. Mater. Sci. Technol.*, 2020, **55**, 35–55.

26 A. Benedetto Mas, S. Fiore, S. Fiorilli, F. Smeacetto, M. Santarelli and I. Schiavi, *Sustainability*, 2022, **14**, 3335.

27 S. Saffirio, S. Pylypko, S. Fiorot, I. Schiavi, S. Fiore, M. Santarelli, D. Ferrero, F. Smeacetto and S. Fiorilli, *Sustainable Mater. Technol.*, 2022, **33**, e00473.

28 S. Sarner, N. H. Menzler, A. Hilgers and O. Guillon, *ECS Trans.*, 2023, **111**, 1369–1378.

29 C. Lei, I. Aldous, J. M. Hartley, D. L. Thompson, S. Scott, R. Hanson, P. A. Anderson, E. Kendrick, R. Sommerville, K. S. Ryder and A. P. Abbott, *Green Chem.*, 2021, **23**, 4710–4715.

30 A. Urushibara, Y. Moritomo, T. Arima, A. Asamitsu, G. Kido and Y. Tokura, *Phys. Rev. B: Condens. Matter Mater. Phys.*, 1995, **51**, 14103–14109.

31 J. Schindelin, I. Arganda-Carreras, E. Frise, V. Kaynig, M. Longair, T. Pietzsch, S. Preibisch, C. Rueden, S. Saalfeld, B. Schmid, J. Y. Tinevez, D. J. White, V. Hartenstein, K. Eliceiri, P. Tomancak and A. Cardona, *Nat. Methods*, 2012, **9**, 676–682.